Journal of Applied Fluid Mechanics, Vol. 17, No. 1, pp. 105-115, 2024.
Available online at www.jafmonline.net, ISSN 1735-3572, EISSN 1735-3645.
https://doi.org/10.47176/jafm.17.1.2038

Analysis of Near-wall Coherent Structure of Spiral Flow in Circular Pipe Based on Large Eddy Simulation

Z. Wang[1], Y. Yin[1], S. Li[1†], Y. Xu[1], L. Li[1,2] and G. Li[1]

[1]*The Mechanical scientific and engineering college of Northeast Petroleum University, Daqing, Heilongjiang Province, 163318, China*
[2]*Oil Recovery Plant No. 3 of Daqing Oilfield Company Limited, Daqing 163113, China*

†Corresponding Author Email: lisen20021225@126.com

ABSTRACT

Based on the large eddy simulation method, this study performed the three-dimensional transient numerical analysis of the near-wall flow field of the spiral flow in a circular pipe and applied the sub-grid model of the kinetic energy transport. The low-speed bands, streamwise vortices and hairpin vortices of the spiral flow in the near-wall region of the circular pipe are determined using the Q criterion. The ejection and sweeping of coherent structures are identified using the velocity vector of the near-wall region; moreover, the two methods of creating the hairpin vortices are established by the image time series. The results demonstrate that the development directions of the near-wall bands, streamwise vortices and hairpin vortices of the spiral flow in the circular pipe develop along the path of the spiral line. The average spanwise period of the low-speed bands in the near-wall region is approximately 120 wall units, the length is more than 900 wall units and the height is not more than 40 wall units. The separation distance of the streamwise vortices is about 119 wall units. It has a certain angle with the wall (approximately 22°). The average burst period of a hairpin vortices is less than 0.015 s.

Article History

Received May 28, 2023
Revised August 16, 2023
Accepted August 24, 2023
Available online November 1, 2023

Keywords:

Coherent structure
Large-eddy simulation
Near-wall turbulence
Spiral flow
Q criterion

1. INTRODUCTION

The spiral flow of a circular pipe is frequently used in petrochemical and environmental protection industries and has been a hot topic in fluid mechanics research. In several fluid machines, the stability of the spiral flow of a circular pipe is a crucial indicator of its efficient operation. Contemporary investigations on the spiral flow of circular pipes primarily focus on the distribution law of the velocity and pressure fields. Zeng & Yong (2011) used the large eddy simulation (LES) model to numerically simulate the spiral flow in a hydrocyclone. They determined the distribution rule of pressure, velocity and turbulent kinetic energy. The simulation results closely match the experimental results. Lim et al. (2010) applied the LES model and particle image velocimetry (PIV) test technology to achieve a satisfactory prediction of the spiral flow field of the hydrocyclone. Delgadillo & Rajamani (2005) used LES to simulate the spiral flow of a circular pipe. Their findings demonstrated that the LES model could achieve a very accurate velocity distribution, especially while predicting tangential velocity. Xu et al. (2018) used PIV technology to measure the spiral flow in conical pipes under vibration and obtained its flow characteristics. Ram & Kumar (2014) performed a numerical simulation of the swirling flow field. Flow characteristics, including velocity and temperature profiles and boundary layer displacement thickness, are examined for various magnetic field–dependent (MFD) viscosity values and suction parameters. Meng et al. (2020) utilised numerical simulation methods to analyse the effects of the geometric shapes of the spiral separator on the flow film's thickness, flow pattern and flow pattern of the spiral separator. The above research primarily focuses on analysing the spiral flow field characteristics and simulation methods, and there is currently little research on drag reduction in spiral flow.

NOMENCLATURE

ρ	density of the fluid	Δ_f	filter width
u_i	velocity vector	V	Volume
x_i	ith spatial coordinate	k_{sgs}	subgrid-scale kinetic energy
t	time	C_k	constants
p	kinematic pressure	C_ε	constants
v	kinematic viscosity	σ_k	coefficient
τ_{ij}	sub-grid scale stress	S_{ij}	strain rate tensor
τ_{kk}	isotropic part of the subgrid-scale stresses	W_{ij}	rotation rate tensor
μ_t	subgrid-scale turbulent viscosity	Φ	physical quantity
$\bar{S}_{ij}$	strain rate tensor	$\Phi^{(m)}$	Flow physical quantity
δ_{ij}	Kronecker delta		

Turbulent frictional resistance is an important factor causing tangential velocity retardation of spiral flow. Currently, the research on coherent structure focuses mostly on the turbulence in the near-wall area, such as typical pipe flow and channel flow. Previous research has revealed that the formation of turbulent frictional resistance is directly connected to the coherent structure of turbulence (Xu, 2015). Jiménez et al. (2010) calculated and analyzed the channel flow with Re_θ<2100. They discovered a modest number of hairpin vortex structures in the research findings. Pan et al. (2009) used PIV to measure the fully developed turbulent boundary layer, and applied the finite-time Lyapunov exponent method to identify the coherent structure of the measured velocity field. It was found that the generalized horseshoe vortex structure is a typical Lagrangian coherent structure in the turbulent boundary layer. Wu (2010) used DNS to simulate the flat turbulent boundary layer with Re_θ=1800, and obtained the hairpin vortex structure at different flow directions in the boundary layer. Baltzer et al. (2013) achieved large/super large scale structure using a direct numerical simulation of turbulence in a circular pipe with Re=685. Dai et al. (2019) employed direct numerical simulation and large-eddy simulation to investigate the impact of streamwise rotation on turbulent channel flow. The mean shear of the channel flow is shown to have an influence on the tilting of large-scale vortical structures and the preference of their distributions in the channel.

Tyagi & Acharya (2003) used the LES method to predict the near-wall coherent structure with high Reynolds numbers of turbine blades. Qin et al. (2012) obtained a large-scale turbulent coherent structure in the engine cylinder, based on LES and combined with the vortex structure identification method. Zhong et al. (2019) used the large eddy simulation numerical approach to investigate the natural shedding frequency of the near-tail vortex of a disc with Re = 22000. Abe et al. (2023) investigated the periodic release of multiple spreading homogeneous vortex structures in the front separation flow of an airfoil with a Reynolds number of 63000 and an Angle of attack of 12 degrees, and the results of the study provide a basis for a fast and smooth turbulence transition in the airfoil. Chen and He (2022, 2023) accurately predicted the development features of near-wall coherent structures utilising the LES and the two-scale research approach, using a refined mesh in the near-wall region and a global coarse mesh in the mainline region.

At present, the existing literature is full of coherent structure research on the cylindrical gas-water circulation flow (Fard et al., 2020), the spiral finned tubes flow in the heat exchanger (Yuan et al., 2022), and the vortices flow (Liu & Zhou, 2022a). These studies provide the foundation and reference for analysing the internal fluid flow characteristics and structural optimisation. Examining the coherent structure of spiral flow in circular tubes is also helpful. This paper examines the LES of the spiral flow in a circular pipe and preliminarily discusses the evolution mechanism of coherent structure in the near-wall region. The fine structure and coherent structure bursting processes of turbulent flow fields such as low-speed bands, streamwise vortices and hairpin vortices of spiral flow in the near-wall region of the circular pipe are identified using the Q criterion, and two mechanisms of the formation of a hairpin vortex are analysed.

2. MATHEMATICAL AND PHYSICAL MODEL

2.1 Geometric Models and Flow Characteristics

Considering the full development of internal fluids within the structure, the study object is a tangential entry with a four prism inlet construction, and the diameter D of the circular tube is 14 mm. The specific structural parameters are shown in Table 1. In this paper, when the inlet velocity is 0.5 m/s, the fluid flow in the circular tube remains constant. When the fluid enters the circular pipe from the tangential inlet, the fluid rotates and flows along the axial direction of the

Table 1 Geometrical dimensions of the calculation models

L	a	b	c	β
10.0D	1.29D	0.36D	0.36	15°

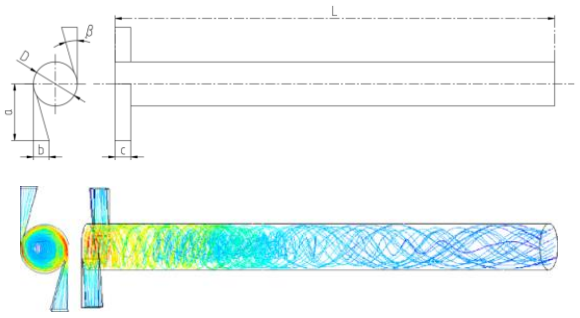

Fig. 1 Geometric models and flow diagrams

circular pipe. As the rotational velocity of the spiral flow along the axial direction gradually decreases, it tends to be stable at the end of the tube, as seen in Fig. 1.

The numerical simulation of the near-wall coherent structure of the spiral flow of a circular pipe is conducted in this paper. However, few reports on the near-wall coherent structures of the spiral flow of the circular pipe have been published. The research results heavily emphasise on the internal flow field of the spiral flow of the circular pipe. The method is applied to observe the adaptability of the LES for investigating the spiral flow field. Delgadillo & Rajamani (2007) used the large eddy model to perform numerical simulation and experimental research on the hydrocyclone. They validated the reliability of the large eddy model, such as axial velocity and tangential velocity of the flow field values.

Saidi et al. (2012) compared and analyzed the large eddy model with other turbulence models for the hydrocyclone, and the analysis results showed that the large vortex model was in good agreement with the existing experimental velocity values, proving the large eddy model's applicability to the spiral flow field.

Misiulia et al. (2021) used LES model to simulate spiral flow and obtained the fluctuation of pressure loss with Reynolds number.

Wang et al. (2022) applied the LES model to investigate the development of rotational flow vortex structures in both axial and radial directions, with vortex damage mainly occurring in the upstream region. And the rationality of LES model for predicting spiral flow was verified through experimental analysis.

The coherent structures are vastly reported in plates, channels and tubes. Combined with the above discussion and present research status, the LES method obtains relatively reliable prediction results in both high Reynolds and low Reynolds numbers. Therefore, this paper intends to apply the LES method to examine the near-wall coherent structure of the spiral flow of the circular pipe.

2.2 Governing Equation Large Eddy Simulation

We consider an incompressible fluid of kinematic viscosity v in motion with kinematic pressure p and velocity $u_i=(u,v,w)$ along Cartesian axes $x_i=(x,y,z)\in\Omega$, Ω within some domain $\Omega\in R^3$. The fluid domain medium uses water, with density of 998.2 Kg/m^{3}and viscosity of $0.001P_a{\cdot}s$. The governing equations of the large eddy model are as follows (Bagheri et al., 2019):

$$\frac{\partial \rho}{\partial t}+\frac{\partial}{\partial x_i}\left(\rho \bar{u}_i\right)=0 \tag{1}$$

$$\frac{\partial}{\partial t}\left(\bar{u}_i\right)+\frac{\partial}{\partial x_j}\left(\bar{u}_i\bar{u}_j\right)=-\frac{1}{\rho}\frac{\partial \bar{p}}{\partial x_i}+\nu\frac{\partial^2 \bar{u}_i}{\partial x_j \partial x_j}-\frac{\partial \tau_{ij}}{\partial x_j} \tag{2}$$

$$\tau_{ij}=\overline{u_i u_j}-\bar{u}_i\bar{u}_j \tag{3}$$

Where τ_{ij} represents the sub-grid scale stress (SGS stress) (Liu & Zhou, 2022b), which reflects the effect of the motion of the small-scale vortex on the solution of the equation. To close the computational model, the SGS stress is estimated using the Boussinesq hypothesis:

$$\tau_{ij}-\frac{1}{3}\tau_{kk}\delta_{ij}=-2\mu_t\bar{S}_{ij} \tag{4}$$

$$\bar{S}_{ij}\equiv\frac{1}{2}\left(\frac{\partial \bar{u}_i}{\partial x_j}+\frac{\partial \bar{u}_j}{\partial x_i}\right) \tag{5}$$

Where μ_t represents the SGS turbulent viscosity and $\bar{S}_{ij}$ represents the strain rate tensor.

The filter function is crucial in realising the large eddy simulation equation. The large eddy and the small eddy can be distinguished by the filter function can. $f(x,t)$ is any instantaneous flow variable, and its large scale can be described by the following weighted integral in the physical space region:

$$\bar{f}(x,t)=\int_D f(x',t)G(x-x',t,\Delta_f)dx' \tag{6}$$

In the formula, $G(x\text{-}x',t,\Delta_f)$ is the filter function; Δ_f is the filter width;

$G(x\text{-}x',t,\Delta_f)$ determines the scale of solving vortices. Because the standard structured mesh is used in numerical simulation, and the computational model is larger and the computational time is longer, the Top-hat filter function is more suitable for spiral flow in a circular pipe. It is expressed as follows:

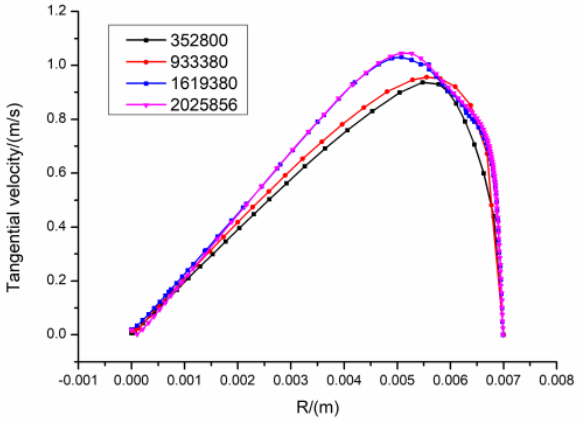

Fig. 2 Comparison of the tangential velocity simulated with different meshes

$$G\left(x-x',t,\Delta_f\right)=\begin{cases}1/V & x-x'\in V\\ 0 & x-x'\notin V\end{cases} \tag{7}$$

The filtering function is to take an average value of a physical quantity in a control volume V.

For the accuracy of the numerical calculation, the Sub-Grid Scale function (SGS) in the large eddy simulation calculation equation is crucial. The small-scale vortices in the region around the wall account for a significant percentage of the energy described by the Sub-Grid Scale model. The Kinetic-Energy Transport (KET) is more appropriate for spiral flow and can collect more information on the wall since the characteristic scale of flow in the near-wall area of pipes is quite tiny. KET is therefore utilized in this paper.

$$\tau_{ij}-\frac{2}{3}\rho k_{sgs}\delta_{ij}=-2C_k\rho k_{sgs}^{1/2}\Delta\bar{f}\bar{S}_{ij} \tag{8}$$

Where, k_{sgs} can be obtained by solving the following transport equation:

$$\rho\frac{\partial\bar{k}_{sgs}}{\partial t}+\rho\frac{\partial\bar{u}_j\bar{k}_{sgs}}{\partial t}=-\tau_{ij}\frac{\partial\bar{u}_i}{\partial x_j}-C_\varepsilon\rho\frac{k_{sgs}^{3/2}}{\Delta f}+\frac{\partial}{\partial x_j}\left(\frac{\mu_t}{\sigma_k}\frac{\partial k_{sgs}}{\partial x_j}\right) \tag{9}$$

In the above equations, the model constants, C_k and C_ε, are determined dynamically (Kim, 2013). σ_k is hardwired to 1.0.

2.3 Mesh of Computational Domain and Boundary Conditions

A mesh-dependent analysis of the tangential velocity is performed because of the spiral flow in the circular pipe. Figure 2 demonstrates the tangential velocity of the different meshes at 80 mm from the entrance in the radial distribution. The figure shows that the velocity mostly overlaps when the number of meshes exceeds 1,619,380. This study used a mesh number of 2,025,856 for subsequent research to ensure the reliability of the following research data.

The structural parameters of the spiral flow calculation domain in a circular pipe are dimensionless, and the size of the calculation domain is 1728 v_w/u_τ × 278 v_w/u_τ × 5073 v_w/u_τ (circumferential direction × radial direction × axial direction). The number of mesh nodes in the three directions is 96 × 80 ×267, respectively. It is evenly distributed in the circumferential and axial directions. In contrast, the near-wall area in the radial direction is present as refinement (Fig. 3).

The mesh height of the initial layer is computed as follows (Kuraishi, 2022):

$$y=\frac{y^+\mu}{U_\tau\rho} \tag{10}$$

taking y+ = 0.5, the mesh height of the first layer is L = 0.005 mm. The mesh scale is expanded by a scale factor of 1.03 in the radial direction, and 11 points are included in the range of y+<10; x+=18 and z+=19. The whole computational domain is a hexahedral mesh with

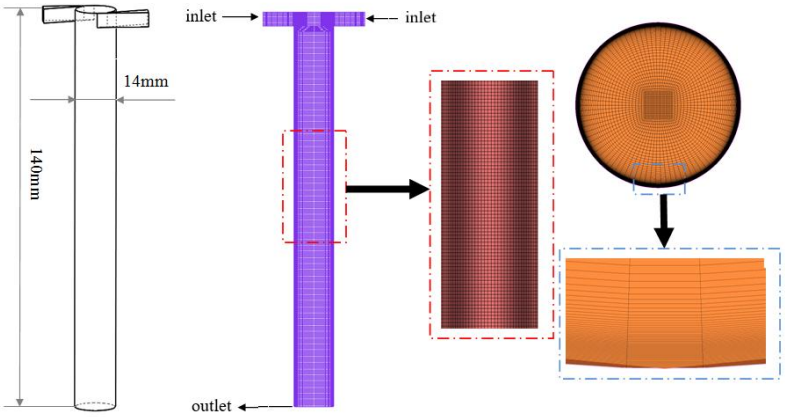

Fig. 3 Graphics of calculation domain and mesh view

Table 2 Spatial discretization and precision

Simulation method	LES
Pressure-velocity coupling method	PISO proximity correction
Gradient interpolation	least square method
Pressure interpolation	Standard
Convection interpolation	Second Order Upwind
convergence precision	1×10^{-5}
SGS	KET
Time step	0.005 s

A total mesh of 2.0 × 10^6, which can ensure the accurate capture of small-scale flow structures in the flow field. In this paper, the Reynolds number of the flow field is 13,933.

The mesh spacing and Reynolds values are referred to in the channel flow study in a previous study (Eriqitai Zou et al., 2004). The velocity of the inlet is 0.5 m/s, the turbulent intensity is 5.6%, the hydraulic diameter is 5 mm, the bottom outlet is set as outflow, and the wall non-slip boundary condition is applied. The calculation is completed based on Fluent software.

2.4 Discrete Schemes and Algorithms

To achieve computational stability as soon as possible, the *k-w* model is used to solve a steady flow field at first, and the transient results of the *k-w* model are taken as the initial values of large eddy simulation. The governing equation is discretized by the finite volume method in the computational domain. The specific parameters are shown in Table 2.

3. COHERENT STRUCTURE ANALYSIS METHOD

The large-scale coherent structure in the spiral field generally takes the form of a vortex. To more clearly visualise the vortex characteristics in the flow field, the *Q* criterion method can be used to identify the vortex structure. The *Q* criterion discriminant approach is based on the quadratic invariant of the velocity gradient tensor to study the evolution of the vortex structure in the flow field (Bedrouni et al., 2020). The velocity gradient tensor can be decomposed into two parts: symmetric and asymmetric. Those parts are described as follows:

$$S_{ij}=\frac{1}{2}\left(\frac{\partial u_i}{\partial y}+\frac{\partial u_j}{\partial x}\right) \tag{11}$$

$$W_{ij}=\frac{1}{2}\left(\frac{\partial u_i}{\partial y}-\frac{\partial u_j}{\partial x}\right) \tag{12}$$

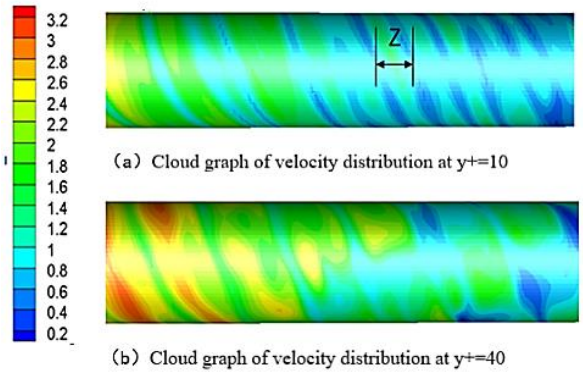

Fig. 4 Velocity and vorticity distribution of the viscous sub-layer（t=2.9500

Q criterion is a quadratic invariant of the velocity gradient tensor, which is defined as follows:

$$Q=\left(W_{ij}W_{ij}-S_{ij}S_{ij}\right) \tag{13}$$

where *Q* represents the degree to which the rotation rate $W_{ij}W_{ij}$ exceeds the strain rate $S_{ij}S_{ij}$. In the region of $Q > 0$, compared with the strain rate $S_{ij}S_{ij}$ of fluids, the rotation rate $W_{ij}W_{ij}$ is dominant, indicating the prevalence of the vortex structure in the region.

4. ANALYSIS OF CALCULATION RESULTS

4.1 The Band Structure in The Near-wall Region

Figure 4 depicts the low-speed band distribution that is parallel to the wall. Near the wall region, the low-speed fluid forms an elongated strip shape and exhibits a certain periodicity in the spanwise direction. With the increased distance from the wall, the low-speed band gradually becomes shorter, and the spacing becomes larger. When the distance from the wall is increased to 40 wall units, the low-speed region is displayed in a group, and the brand starts disappearing. The development process of the low-speed brand is similar to the channel flow and the circular pipe axial flow. Moreover, the difference is that the direction of the spiral flow band is not along the axial direction but along the direction of the velocity streamline. The low-speed bands in the near-wall region are statistically averaged (Fig. 4 (a)). Figure 4(c) depicts the vorticity distribution at the position y+ = 10, and the low-speed strip occupies about 6.3 grids on average (Shi, 2012). Figure 4 shows that the average strip spacing (average spanwise period) *Z* is about 6.3 × 19 wall units ≈ 120 wall units. The low-speed band is almost continuous under the y+ = 10 position. With the development of the flow direction, the strip structure will undergo a certain fracture, but the length is still greater than half the circumference of the pipe; for example, the low-

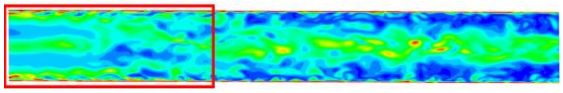

(a) The global vorticity diagram

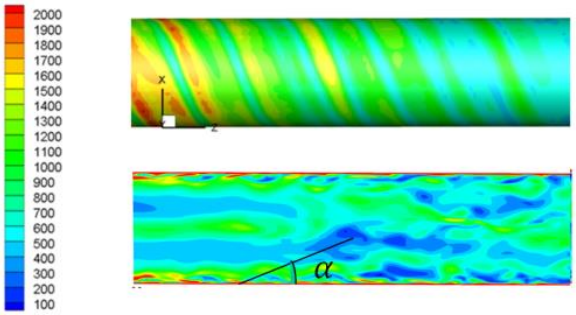

(b) The local vorticity diagram

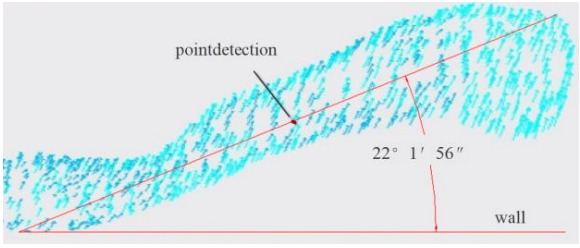

(c)Side view of the iso-vorticity surfaces

Fig. 5 Vorticity distribution（t=2.9500）

speed brand length is greater than 900 wall units. Figure 4 (a) and (b) show that the distribution of the low-speed band is significantly different from y+=10 when the height exceeds y+=40, and the flow structure becomes chaotic. Thus, it can be shown that the speed brand exists in the region under the height of 40 wall units.

4.2 The Development of Streamwise Vortices

In the near-wall region of the spiral flow of the circular pipe, the streamwise vortices plays a vital role in generating turbulent energy transport and developing turbulence in the boundary layer. Figure 5 presents the distribution of the iso-vorticity surface. In the near-wall region, the streamwise vortices iso-surface and the vortex criterion region have a one-to-one correspondence and the same trend (Fukagata et al., 2002). To quantitatively determine the morphological change of the streamwise vortices, the flow field physical quantity Φ (x, y, z) is conditionally averaged for the positive streamwise vortices (Ge et al., 2012).

$$\left\langle \phi(\Delta x, y, \Delta z) \right\rangle^{P} = \frac{1}{N_P} \sum_{m=1}^{N_P} \phi^{(m)}(\Delta x, y, \Delta z) \tag{14}$$

The conditional mean result reflects the average statistical form of the streamwise vortices at the central point at y+=20. FIG. 5(c) displays the top view of the

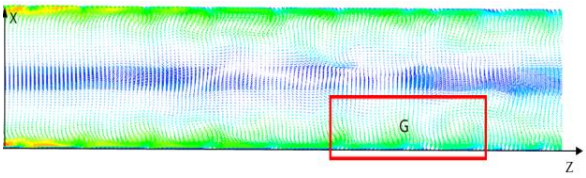

(a) The global velocity vector diagram

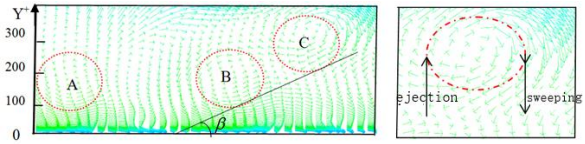

(b) The locally amplified diagram of section G and The diagram of vortex head at section C

Fig. 6 Near-wall velocity vector（t=2.9500）

streamwise vortices iso-surface with iso-surface 1 based on the above formula. Along the flow direction, the distribution of the iso-vorticity surface is similar and has a specific uplift relative to the wall. It has a specific angle with the wall (about 22°). The iso-vorticity surfaces exhibit thin ribbons and high-low interlaces in the flow direction. The distribution trend of the streamwise vortices is similar to the channel flow and the circular pipe axial flow. Furthermore, the difference means that the direction of the vorticity line is not along the axial direction but along the path of the velocity streamline. As the flow field develops downstream, the vorticity decreases, and the thin ribbon of the streamwise vortices gradually vanishes due to the large-scale vortices structure beginning to break into the small-scale vortices. Because the tail of the streamwise vortices is closer to the wall surface, it can act on the wall surface more effectively and create a higher wall friction resistance. Fig.5 (a) shows the spatial structure of the streamwise vortices.

4.3 The Ejection and Sweeping of Coherent Structure

The fluid's ejection and sweeping are among the most crucial turbulence flow phenomena in the boundary layer near the wall. Various studies have demonstrated that the bursting process of sweeping high-speed fluid and the ejection of low-speed fluid are the sources of Reynolds shear stress in the near-wall region. Figure 6 (a) shows the global velocity vector diagram. The figure shows a continuous velocity vortex in the near-wall region. Figure 6 (b) illustrates the locally amplified vector diagram of some vortex groups. The velocity vortex is gradually thrown up and away from the wall surface along the direction of flow direction, forming an angle (about 24°) with the wall surface. These vortex groups are the vortex heads of the hairpin vortices. Fig. 6 (b) also shows that the outer layer of high-speed fluid in the near-wall region rushes into the inner layer. In contrast, the inner layer of low-speed fluid ejects outward (the phenomenon of ejection

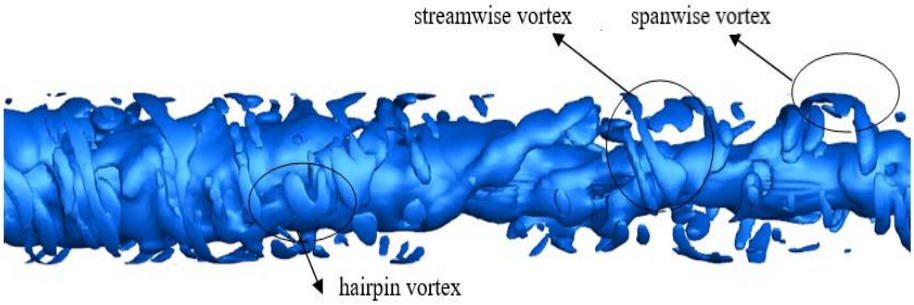

(a) Whole vortex structure diagram

(b)local hairpin vortex structure diagram

Fig. 7 Coherent structure diagram（t=2.9500）

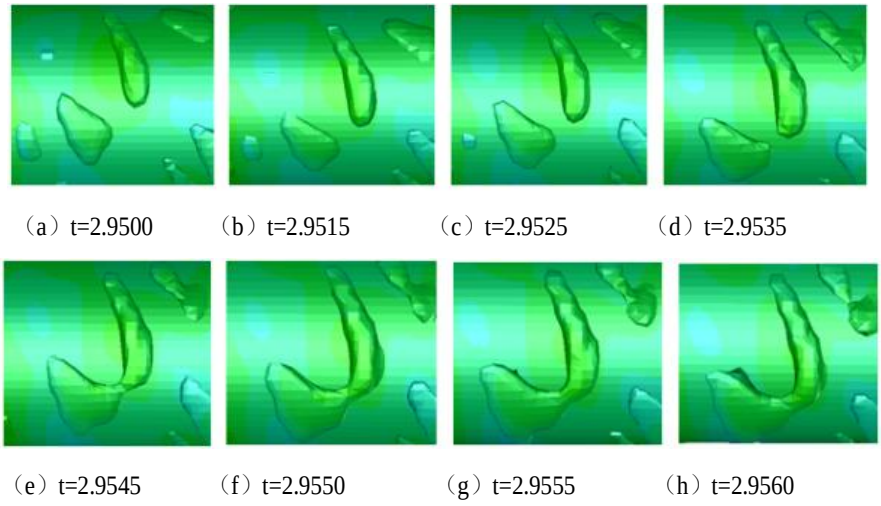

（a）t=2.9500 （b）t=2.9515 （c）t=2.9525 （d）t=2.9535

（e）t=2.9545 （f）t=2.9550 （g）t=2.9555 （h）t=2.9560

Fig. 8 Evolution process of the hairpin vortex formed with a pair of streamwise vortex

and sweeping). The entire process is called a burst.

4.4 Spatial Evolution of Coherent Structures

When the standard *Q* value is 0.1, the coherent structure of a spiral flow in a circular pipe can be identified (Fig. 7 (a)). Figure 7 (a) shows the streamwise, spanwise, and hairpin vortices. Figure 8 (b) shows the amplified hairpin vortex structure. The width of the spanwise vortex occupies about three mesh points. Hence, the separation distance of the streamwise vortices is about 119 wall units, which is consistent with the spanwise period of the low-speed band. The streamwise vortices also develops in the direction of the spiral flow line. The above description shows that the development of the streamwise vortices in a spiral flow corresponds to the low-speed band.

Figure 8 illustrates the formation of a hairpin vortex by symmetrical streamwise vortex pairs at y+ >40 in. When two adjacent streamwise vortex pairs are close to each other, the heads of the two streamwise vortices are stretched until they slowly overlap, creating a bridge-like spanwise vortex structure that merges into a hairpin vortex structure. The “bridging” of the streamwise vortices pairs generates this process of creating a hairpin vortices. The formation process of the generated hairpin vortices structure is consistent

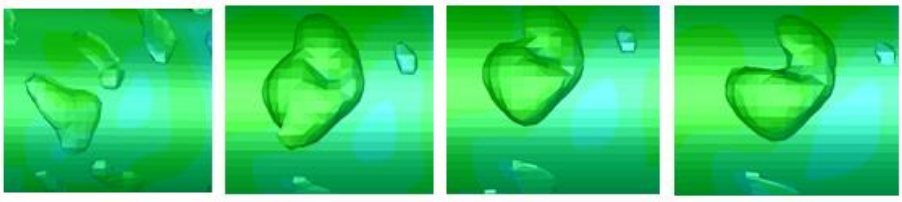

（a）t=2.9530 （b）t=2.9590 （c）t=2.9600 （d）t=2.9620

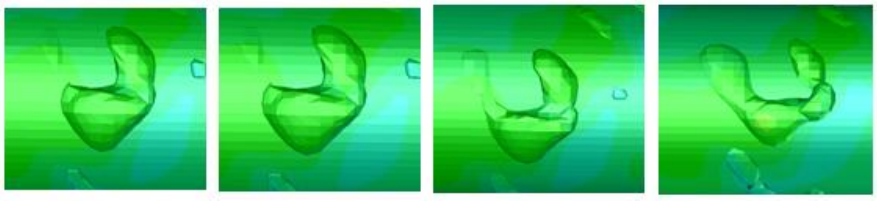

（e）t=2.9630 （f）t=2.9640 （g）t=2.9650 （h）t=2.9680

Fig. 9 Evolution process of the hairpin vortex from a single streamwise vortex

with the literature (Chen et al., 2009).

When the two streamwise vortices are close to each other, the hairpin vortex as mentioned above will appear, but not all streamwise vortices are close to each other, nor can all streamwise vortices close to each other merge to create a new hairpin vortex. Therefore, the second formation method of the hairpin vortex is also familiar: the process of a single-flow vortex gradually developing into a hairpin vortex. Figure 9 depicts the operation of the streamwise vortices inclined along the direction of the spiral flow streamlines that develop into a hairpin vortices. Figure 9 (a) shows the streamwise vortices. The head part of the streamwise vortices is close to the wall under its action and progresses towards the spanwise direction simultaneously. Its vortices head stretches towards the spanwise direction and creates the spanwise vortices. This event is similar to the formation process of the hairpin vortices with one-sided vortex legs, as described by Robinson (1991). The generated spanwise vortices continues to develop in the direction of the streamwise direction. The vortex leg evolves from a single to a double leg, and the newly formed vortices legs continue to elongate and become thinner (Fig. 9 (c)–(f)). According to statistics, the average burst period of the hairpin vortices is below 0.015s.

The above analysis demonstrates that the formation and evolution mechanism of the near-wall coherent structure of the spiral flow of the pipe is similar to the form of the coherent structures of the channel flow and the tube flow, including their scale. The difference is that the cohesive structure of the spiral flow of the pipe does not develop in the axial direction like the coherent structure of the tube flow but at an angle to the axial direction.

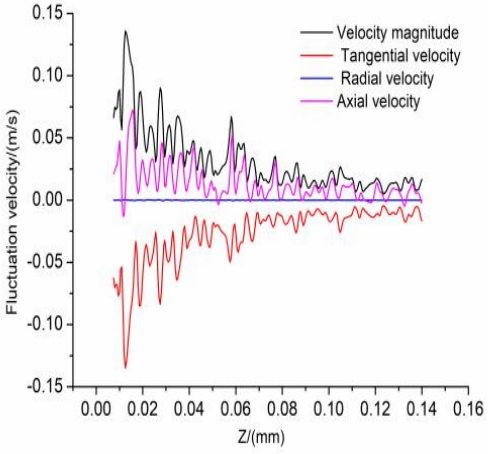

Fig. 10 Distribution of pulsation velocity along axial distance

4.5 Fluctuation Velocity Distribution

Figure 10 illustrates the axial distribution of fluctuation velocity in the near-wall area. The fluctuation velocity gradually decreases along the axial direction. The maximum fluctuation velocity is about 0.14, and the smallest is 0.01. The amplitude of fluctuation velocity in the *y*-axial direction is the smallest, close to 0, and the tangential fluctuation velocity energy is the strongest.

4.6 Reynolds Stress Distribution

Figures 11-13 shows the Reynolds stress distribution at different sections (z=80, 90, 100, 110, 120). Where, u'', v'' and w'' represents the fluctuation velocity values in the three coordinate directions, The symbol〈 〉represents the mean value.

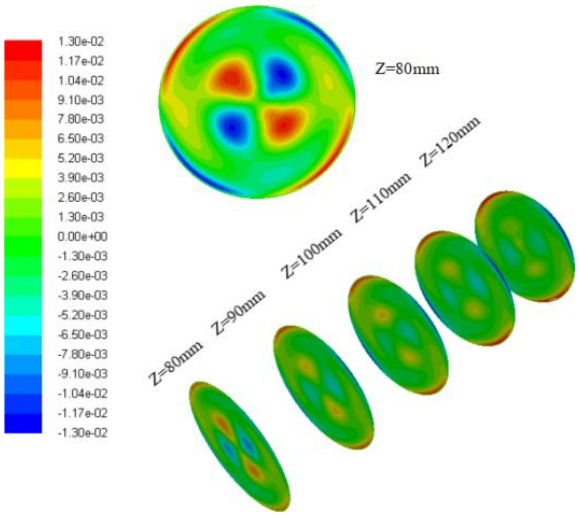

Fig. 11 ⟨*u″v″*⟩ distribution at different sections

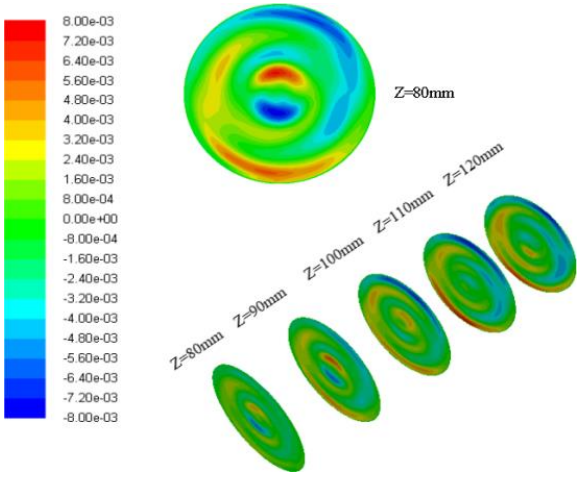

Fig. 12 ⟨*u″w″*⟩ distribution at different sections

Figure 11 shows the distribution of ⟨*u″v″*⟩ at different cross-sections. It can be seen that the maximum value of ⟨*u″v″*⟩ is in the near-wall region rather than in the mainstream region, and that as axial distance increased, the value of ⟨*u″v″*⟩ decreased significantly in the main flow area. However, the ⟨*u″v″*⟩ in the near-wall area decreases slowly and the maximum position remains constant. And the value of ⟨*u″v″*⟩ is significantly larger than the Reynolds stress values in the other two directions.

It can be seen from Fig. 12 that the maximum value of ⟨*u″w″*⟩ *uv* also be detected in the near-wall region. With the increase of axial distance, the value of ⟨*u″w″*⟩ decreases significantly in the near-wall region, and the maximum value remains unchanged.⟨*v″w″*⟩ and ⟨*u″w″*⟩ values have similar variation rules, as shown in Fig. 13 (c), except that the value of ⟨*v″w″*⟩ in the near-wall region is the smallest.

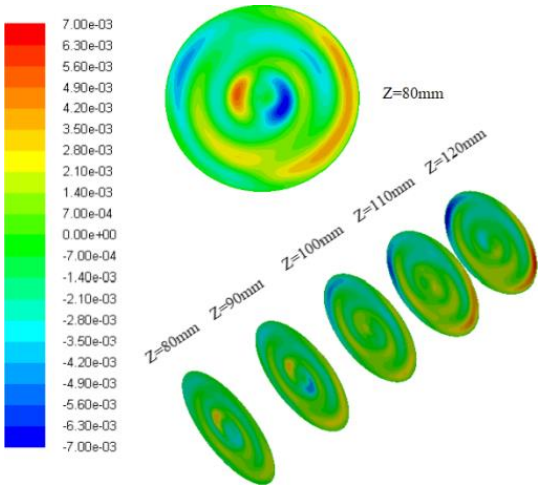

Fig. 13 ⟨*v″w″*⟩ distribution at different sections

The above analysis shows that the maximum Reynolds stress in the spiral flow field of the circular pipe appears in the near-wall region, and the wall shear force is stronger and fluctuates in the tangential and axial directions. The increased tangential and axial velocities in the spiral flow of the circular tube, as well as the larger fluctuation of the tangential and axial velocities, are primarily responsible for this. The *UV* and *UW* Reynolds stresses have a significant impact on the bursting of the spiral flow's near-wall coherent structure.

5. CONCLUSION

1) The LES combined with the *Q* criterion can be used to identify the coherent structure of the near-wall flow field of a spiral flow in a circular pipe. The results demonstrate that the development directions of the low-speed bands, streamwise vortices and hairpin vortices of the spiral flow in the circular pipe develop along the spiral line direction.

2) The average spanwise period of the low-speed bands in the near-wall region is approximately 120 wall units, the length is more than 900 wall units and the height is not more than 40 wall units.

3) The streamwise vortices are in the shape of thin ribbons and high-low interlaces. Along the flow direction, the distribution of the iso-vorticity surface is similar, and there is a specific uplift. The angle between the streamwise vortices and the wall surface is certain (about 22°). The separation distance between the streamwise vortices is about 119 wall units, which is consistent with the spanwise period of the low-speed band.

4) The formation of hairpin vortices of spiral flow in a circular pipe can be divided into two types:

(a) The hairpin vortices are generated by the "bridging" of streamwise vortices on the head; (b) Under the self-induced action, the vortex head of a single streamwise vortices develops in a spanwise direction and evolves into two vortices legs to create a hairpin vortices. The burst period of the hairpin vortices is below 0.015 s.

5) The maximum Reynolds stress in the spiral flow field of the circular pipe appears in the near-wall region, and the wall shear force is more robust in the tangential and axial directions. The *UV* and *UW* Reynolds stress significantly affect the bursting of the near-wall coherent structure of the spiral flow.

ACKNOWLEDGMENT

This work was supported by the project of Nature Scientific Foundation of Heilongjiang Province (LH2022E016, LH2022A004).

CONFLICT OF INTEREST

The authors declared no potential conflicts of interest with respect to the research, authorship, and/or publication of this article.

AUTHORS CONTRIBUTION

Zunce Wang: Conceptualization, overall planning, investigation; **Yifang Yin**: methodology, formal analysis, writing-original draft preparation; **Sen Li**: writing-review and editing; **Yan Xu**: validation, data curation; **Lidong Li**: software, visualization; **Guobao Li**: Writing-Review & Editing.

REFERENCES

Abe, Y., Nonomura, T., & Fujii, K. (2023) Flow instability and momentum exchange in separation control by a synthetic jet. *Physics of Fluids, 35*, 065114. https://doi.org/10.1063/5.0148943

Bagheri, M. H., Esmailpour, K., Hoseinalipour, S. M., & Mujumdar, A. S. (2019). Numerical study and POD snapshot analysis of flow characteristics for pulsating turbulent opposing jets. *International Journal of Numerical Methods for Heat & Fluid Flow*, *29*(6), 2009-2031. https://doi.org/10.1108/hff-07-2018-0382

Baltzer, J. R., Adrian, R. J., & Wu, X. (2013). Structural organization of large and very large scales in turbulent pipe flow simulation. *Journal of Fluid Mechanics*, *720*, 236-279. https://doi.org/10.1017/jfm.2012.642

Bedrouni, M., Khelil, A., Mohamed, B., & Naji, H. (2020). Large eddy simulation of a turbulent flow over circular and mixed staggered tubes' cluster. Journal of *Applied Fluid Mechanics*, *13*(5), 1471-1486. https://doi.org/10.36884/jafm.13.05.31119.

Chen, C., & He, L. (2022). On locally embedded two-scale solution for wall-bounded turbulent flows. *Journal of Fluid Mechanics*, (933), 933. https://doi.org/10.1017/jfm.2021.1075

Chen, C., & He, L. (2023). Two-scale solution for tripped turbulent boundary layer. *Journal of Fluid Mechanics*, (955), 955. https://doi.org/10.1017/jfm.2022.1024

Chen, L., Tang, D. B., Liu, X, B., Oliveira, M., & Liu, C. Q. (2009). Evolution of annular vortices and peak structures during boundary layer transition. *Chinese Science* (*G: Physics Mechanics Astronomy*), *39*(10), 1520-1526. (in Chinese)

Dai, Y., Huang, W. X., & Xu, C. (2019). Coherent structures in streamwise rotating channel flow. *Physics of Fluids*, *31*(2), 021204. https://doi.org/10.1063/1.5051750

Delgadillo, J. A., & Rajamani, R. K. (2005). A comparative study of three turbulence-closure models for the hydrocyclone problem. *International Journal of Mineral Processing*, *77*(4), 217-230. https://doi.org/10.1016/j.minpro.2005.06.007

Delgadillo, J. A., & Rajamani, R. K. (2007). Large-eddy simulation (LES) of large hydrocyclones. *Particulate Science and Technology*, *25*(3), 227-245. https://doi.org/10.1080/02726350701375774

Eriqitai Zou, Z. P., & Wang, Q. (2004). LES of coherent structure in turbulence boundary layer. *Journal of Engineering Thermophysics*. (in Chinese)

Fard, M. G., Vernet, A., Stiriba, Y., & Grau, X. (2020). Transient large-scale two-phase flow structures in a 3D bubble column reactor. *International Journal of Multiphase Flow*, *127*, 103236. https://doi.org/10.1016/j.ijmultiphaseflow.2020.103236

Fukagata, K., Iwamoto, K., & Kasagi, N. (2002). Contribution of reynolds stress distribution to the skin friction in wall-bounded flows. *Physics of Fluids*, *14*(11), L73-L76. https://doi.org/10.1063/1.1516779

Ge, M., Xu, C., Huang, W., & Cui, G. (2012). Drag reduction control based on active wall deformation. *Chinese Journal of Theoretical & Applied Mechanics*, *44*(4), 653-663. https://doi.org/10.6052/0459-1879-11-198

Jiménez, J., Hoyas, S., Simens, M. P., & Mizuno, Y. (2010). Turbulent boundary layers and channels at moderate reynolds numbers. *Journal of Fluid Mechanics*, *657*, 335-360. https://doi.org/10.1017/s0022112010001370

Kim, J. W. (2013). Quasi-disjoint pentadiagonal matrix systems for the parallelization of compact finite-

difference schemes and filters. *Journal of Computational Physics*, *241*, 168-194. https://doi:10.1016/j.jcp.2013.01.046.

Kuraishi, T., Takizawa, K., & Tezduyar, T. E. (2022). Boundary layer mesh resolution in flow computation with the space–time variational multiscale method and isogeometric discretization. *Mathematical Models and Methods in Applied Sciences.* https://doi:10.1142/S0218202522500567.

Lim, E. W. C., Chen, Y. R., Wang, C. H., & Wu, R. M. (2010). Experimental and computational studies of multiphase hydrodynamics in a hydrocyclone separator system. *Chemical Engineering Science*, *65*(24), 6415-6424. https://doi.org/10.1016/j.ces.2010.09.029

Liu, Y., & Zhou, L. (2022a). Hydrodynamic modeling of non-swirling and swirling gas-particle two-phase turbulent flow using large eddy simulation. *Process Safety and Environmental Protection*, *161*, 175-187. https://doi.org/10.1016/j.psep.2022.03.024

Liu, Y., & Zhou, L. (2022b). Numerical analysis on particle dispersions of swirling gas-particle flow using a four-way coupled large eddy simulation. *International Communications in Heat and Mass Transfer*, *133*, 105974. https://doi.org/10.1016/j.icheatmasstransfer.2022.105974

Meng, L., Gao, S., Wei, D., Cui, B., Shen, Y., Song, Z., & Yuan, J. (2020). Effects of cross-sectional geometry on flow characteristics in spiral separators. *Separation Science and Technology*, *56*(17) 2967-2977. https://doi.org/10.1080/01496395.2020.1853169

Misiulia, D., Lidén G., & Antonyuk, S. (2021). Evolution of turbulent swirling flow in a small-scale cyclone with increasing flow rate: a les study. *Applied Scientific Research*, *107*(3), 575-608. https://doi.org/10.1007/s10494-021-00253-2

Pan, C., Wang, J. J., & Zhang, C. (2009). Identification of Lagrangian coherent structures in the turbulent boundary layer. *Science in China Series G-Physics, Mechanics & Astronomy 39*(04), 627-636. (in Chinese) https://doi.org/10.1007/s11433-009-0033-1

Qin, W. J., Xie, M. Z., & Jia, M. (2012). Investigation on engine in-cylinder turbulent flow and coherent structure based on large eddy simulation. *Transactions of Csice*, *30*(2), 133-140. https://doi.org/10.16236/j.cnki.nrjxb.2012.02.011

Ram, P., & Kumar, V. (2014). Swirling flow of field dependent viscous ferrofluid over a porous rotating disk with heat transfer. *International Journal of Applied Mechanics*, *06*(04), 1450033. https://doi.org/10.1142/s1758825114500331

Robinson, S. K. (1991) Coherent motions in turbulent boundary layer. *Annual Review of Fluid Mechanics*, *72*, 336-339. https://doi.org/10.1146/annurev.fl.23.010191.003125

Saidi, M., Maddahian, R., Farhanieh, B., & Afshin, H. (2012). Modeling of flow field and separation efficiency of a deoiling hydrocyclone using large eddy simulation. International *Journal of Mineral Processing*, *112-113*(10), 84-93. https://doi.org/10.1016/j.minpro.2012.06.002

Shi, W. L. (2012). Investigation of large eddy simulation and coherent structure for the flow field of turbine vane. *Nanjing: Nanjing university of aeronautics and astronautics.* (in Chinese)

Tyagi, M., & Acharya, S. (2003). Large eddy simulation of film cooling flow from an inclined cylindrical jet. *Journal of Turbomachinery*, *125*(4), 734-742. https://doi.org/10.1115/gt2003-38633

Wang, P., Wei, X., Shrotriya, P., Li, W., & Ferrante, A. (2022). Investigation of isothermal flow inside a new combustor with two-stage axial swirler. *Journal of Applied Fluid Mechanics*, *15*(2), 325-336. https://doi.org/10.47176/jafm.15.02.32653

Wu, X. (2010). Establishing the generality of three phenomena using a boundary layer with free-stream passing wakes. *Journal of Fluid Mechanics*, *664*, 193-219. https://doi.org/10.1017/s0022112010004027

Xu, C. X. (2015). Coherent structures and drag-reduction mechanism in wall turbulence. *Advances in Mechanics*, *45*(1), 111-140. https://doi:10.6052/1000-0992-15-006

Xu, Y., Zhang, Y. Y., Nicolleau, F. C. G. A., & Wang, Z. C. (2018). Piv of swirling flow in a conical pipe with vibrating wall. *International Journal of Applied Mechanics*, *10*(2), 1850022. https://doi.org/10.1142/S1758825118500229

Yuan, M., Zhang, W., Liu, G., Zhang, X., Yousif, M. Z., Song, J., & Lim, H. (2022). Performance study of spiral finned tubes on heat transfer and wake flow structure. *International Journal of Heat and Mass Transfer*, *196*, 123278. https://doi.org/10.1016/j.ijheatmasstransfer.2022.123278

Zeng, R. Q., & Yang, Y. (2011). Numerical simulation of the flow field in oil-water hydrocycolone. *China Petroleum Machinery*. (01), 24-27. https://doi.org/10.16082/j.cnki.issn.1001-4578.2011.01.007

Zhong, W., Yang, J., Zhang, X., Liu Q., & Liu M. (2019). Large eddy simulation of coherent structures of circular-wound flows near wakes. *Journal of Engineering Thermophysics*, 36(2), 308-312. (in Chinese)